Inkjet deposition of liquid-exfoliated graphene and MoS_2 nanosheets for printed device applications

David J. Finn, Mustafa Lotya, Graeme Cunningham, Ronan J Smith, Dave McCloskey, John F Donegan and Jonathan N. Coleman*

School of Physics, CRANN and AMBER, Trinity College Dublin, Dublin 2, Ireland

*colemaj@tcd.ie

Abstract: Here we demonstrate inkjet printing of nanosheets of both graphene and MoS_2 prepared by liquid exfoliation. We describe a protocol for the preparation of inks of nanosheets with well-defined size distribution and concentration up to 6 mg/ml. Graphene traces were printed at low temperature (<70 °C) with no subsequent thermal or chemical treatment. Thin traces displayed percolation effects while traces with thickness above 160 nm displayed thickness-independent conductivity of 3000 S/m. We also demonstrate the printing of semiconducting traces using solvent exfoliated MoS_2. Such traces can be combined with inkjet-printed graphene interdigitated array electrodes to produce all-printed photodetectors.

Keywords: suspension, dispersion, printing, exfoliation, layered compound, photoconductivity.

ToC fig

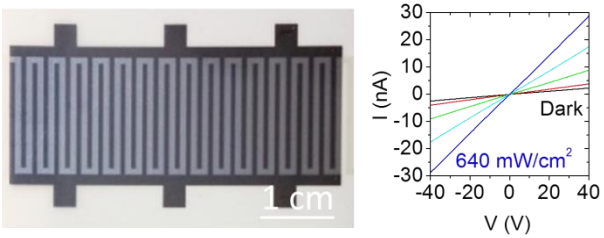

Low temperature inkjet printing of exfoliated nanosheets has been demonstrated leading to conductive graphene traces and all-inkjet printed devices.

Introduction

The field of printed electronics is an emerging technology which is expected to revolutionize the production of low-cost electronic devices. Printed devices have the advantage that they can be fabricated on flexible, transparent substrates and over large areas at relatively low temperatures. Inkjet printing is a non-contact, additive printing process capable of precisely depositing picoliter droplets of functional ink on a substrate in defined patterns.[1] This makes it ideal for the deposition of a range of electronic and optoelectronic materials, including nano-materials for device fabrication. In principle, any material can be deposited so long as it can be dispersed in a liquid. Examples of functional materials which have been inkjet printed are semiconducting[2] and conducting polymers[3], polymer/fullerene mixtures,[4] quantum dots,[5] silver nanoparticles[6] carbon black[7] and carbon nanotubes[8]. These materials have been fabricated into a range of devices including transistors,[9, 10] light emitting diodes,[11] solar cells,[3, 12] supercapacitors,[7, 13] sensors[14, 15] and antennas.[16]

Recently, considerable attention has been given to inkjet printing of inks based on graphene[17, 18] to create functional structures.[19-33] For the most part, these structures have been used as electrodes or other components which rely on the reasonably high conductivity of graphene films.[34] However, many printed electronics applications require low temperature processing. This is a problem because printed graphene structures tend to display relatively low conductivity unless annealed at temperatures of up to 400 °C (see below). When high conductivity has been achieved with low temperature processing, this has been at the cost of using harsh chemical treatments,[28, 29] which may not be compatible with printing of complex devices. Thus, it will be important to develop methods for printing highly conductive graphene structures which do not require high temperature or chemical processing.

In addition, graphene is only one of a large number of 2-dimensional (2D) nanomaterials.[35-40] These materials come in a range of types such as BN, MoS_2 and MnO_2 and display a wide variety of useful properties. For example, 2D materials can be metallic, semiconducting, insulating or superconducting and have novel electrochemical, electronic and opto-electronic properties.[35-37] Many 2D materials can be produced as liquid-dispersed nanosheets via liquid exfoliation of layered crystals.[35] This will certainly facilitate the fabrication of inks which are suitable for printed applications. Indeed, it is likely that there are a wide range of printed device applications where such materials could be incorporated as the active material. Moreover, it is probable that many applications will require the ability to

print combinations of 2D materials, for example a conducting material such as graphene as an electrode and a semiconducting material such as MoS_2, as the active element. Thus, it will be important to demonstrate that a range of 2D materials beyond graphene can be printed both individually and in combinations to form integrated structures.

In this letter, we demonstrate that inks based on solvent-exfoliated graphene can be used to print conductive traces with conductivities as high as 3000 S/m for processing temperatures no higher than 70 °C. We also demonstrate the printing of semiconducting traces using solvent exfoliated MoS_2. Such traces can be combined with inkjet-printed graphene interdigitated array electrodes to produce all-printed photodetectors. We find the interface between MoS_2 and graphene to be extremely uniform and to give apparent Ohmic behaviour. The resultant structure displays reasonable photoconductive properties.

Results & Discussion

In order to achieve good-quality printed structures, it is first necessary to develop appropriate inks and to optimise the inkjet conditions. While many reports have used graphene oxide based inks,[19, 22-24, 26, 28, 29] we favour ink based on defect-free graphene nanosheets. Such nanosheets can be produced by the exfoliation of graphite in solvents,[41-44] aqueous surfactant solutions[45, 46] or solutions of polymers in organic solvents.[47, 48] A number of papers have described inkjetting of such liquid-exfoliated graphene with some success.[25, 27, 31] One particular advantage of these nanosheets is that they require no thermal or chemical treatment to remove oxides.

It is well-known that inkjet printing is optimised for combinations of nozzle diameter, a, and surface tension, γ, density, ρ, and viscosity, η, of the ink such that the inverse Ohnesorge number, $Z = \sqrt{\gamma \rho a} / \eta$, lies within the range: 1<Z<14.[31] However, Torrisi et al. have shown that inks prepared from liquid exfoliated graphene suspended in the solvent N-methyl-pyrrolidone (NMP) can be inkjetted extremely well even when Z is well outside this range.[31] As such, here we focus on inks prepared by exfoliating graphene in NMP as described in a number of papers.[43, 44, 49] However, we found the printing procedure to be sensitive to both the lateral flake size and dispersion concentration with repeated trials showing optimised values of ~170 nm and ~1.6 mg/ml respectively. Smaller flakes give poorly connected films while larger flakes cause clogging of the jetting nozzles. Low concentration dispersions result in low deposited mass per droplet while higher

concentrations are difficult to attain and can cause nozzle blockage. We developed a protocol (see Methods and SI) for producing such dispersions based on a combination of controlled low and high speed centrifugation coupled with re-suspension of sediment. Figure 1A shows a bright-field TEM image of some of the exfoliated graphene nanosheets produced in this way. A histogram showing the lateral flake size distribution is shown in Figure 1B. The nanosheet length follows a broad distribution from 35 nm to ~600 nm with a mean of <L> = 173 nm. Edge analysis[49] shows these flakes to consist of on average 4 stacked monolayers (see SI).

This optimized ink was used to print linear traces on coated PET substrates at relatively low temperature using drop-on-demand inkjet printing. This was achieved using a Dimatix inkjet printer with a printhead consisting of 16 inkjet nozzles with a = 21 μm. Thus, for NMP-based dispersions, $Z = \sqrt{\gamma \rho a} / \eta \approx 17$, came reasonably close to standard inkjet conditions.[31] The traces were fabricated on the coated PET substrate held under vacuum on a heated platen stage in the printer and set to a temperature of 60 °C, while the graphene ink in the actuation chambers of the printhead cartridge was heated to a maximum of 70 °C. After printing, the substrates were left to dry on the printer platen for 1-2 hrs at a maximum temperature of 60 °C.

The trace width, w, and length, L, are controlled by the raster program while the trace thickness, t, is controlled by the drop spacing: diameter ratio, the ink concentration and the number of passes, N. Shown in Figure 1C is a photograph of inkjet-printed traces (w=2 mm, L=20 mm) printed with a range of vales of N from 1 to 30. In this case, the print head raster direction was along the x-axis marked on the Figure. That these traces consist of good quality, defect-free graphene is confirmed by the Raman spectrum shown in Figure 1D (N=30 print passes). The D-band (~1350 cm^{-1}) is relatively small compared to the G-band (~1580 cm^{-1}) consistent with edge rather than basal plane defects.[44, 49] In addition, the 2D-band (~2680 cm^{-1}) is relatively weak and symmetric, consistent with the presence of few-layer graphene.[50]

Figure 1E shows an optical image of the central region of an inkjet-printed line on coated PET after 5 print passes (N.B. this is part of the N=5 line shown in Figure 1C). This clearly shows uniform striations in the print pattern which are aligned in the raster directions (x-axis). These are known as swathe edges in the printing industry and occur along the direction parallel to the ink head raster direction. [51, 52] These features were present at all line

thicknesses. A higher magnification image of the swathe edge is shown in Figure 1F which implies the striation edge to represent a gradual increase in local graphene density.

Figures 1G and 1H show the surface morphology of inkjet-printed graphene lines on coated PET substrates after 20 print passes at high magnification. The images show the traces to be uniform over length scales of tens of microns. However, at smaller length scales, they clearly consist of a disordered array of graphitic nanosheets with lateral dimensions consistent with the TEM data in Figure 1A&B.

In order to fully characterise the printed traces it is necessary to measure their thickness and in particular to understand how the thickness varies with N. In addition, the data in Figure 1 E&F implies the presence of local thickness non-uniformities which must be characterised. To do this we used a Dektak 6M profilometer to measure line scans across the traces (i.e. in the x direction). In all cases, the profiles were measured along the dark striations shown in Figure 1E and so measure peak heights. Figure 2A provides examples of profilometry line profiles for two traces with N=30 and N=40. These profiles reveal reasonably uniform thicknesses along the cross-sections. Figure 2B shows the mean trace height (measured at peak of the striations) plotted as a function of number of passes, N. This data shows the linear dependence of maximum line thickness characterised by t (nm) = (21 ± 1)N.

However, surface probe techniques like profilometry or AFM can be slow and cumbersome. More straightforward are optical measurements of local thickness. A flatbed optical transmission scanner was used to measure the local optical transmission with a spatial resolution of ~5 μm. This technique produces transmission maps that can be presented as images or can be used to extract quantitative local transmission data. Shown in Figure 2C is a transmission map of part of a printed trace (L=20 mm, w=2 mm, N=1). This map clearly shows the dark and light striations (aka swathe lines) described above.

The spatially resolved transmittance data contained in maps such as that in Figure 2C can be transformed to represent absorbance ($A = -\log T$) and line profiles extracted (we present quantitative data in terms of absorbance as it is directly proportional to thickness). Figure 2D shows absorbance line profile taken across the full length of two traces with N=4 and N=8. The inset shows magnified line profiles. It is clear that the apparent “noise” in the main panel can be attributed to thickness variations across striations with a spatial period of

200 μm. The inset of Figure 2D reveals the repeatability of the striation cross sectional profiles. It is clear from this data that the striations introduce a significant thickness variation along the length of the traces. It is important to note that the striation periodicity and bandwidth changed with the print head angle used when printing. In turn, the print head angle was determined by the required drop spacing for printing, in this case 20 μm.

Figure 2E shows the average absorbance, measured both at peak and trough of striations, plotted as a function of number of inkjet passes, N. This data was acquired from averaging the peak and trough absorbance values along the length of the printed lines (z-axis shown in Figure 1A). The data shows a linear scaling of the peak and trough absorbance as a function of N up until an absorbance of approximately 1.5 (T = 3%). The deviation above absorbance 1.5 represents the limitation of the optical scanner's sensitivity. Fitting the linear portion of the data shows that $A_{peak} = (0.150 \pm 0.004)N$. Combining this with the relationship between t and N described above gives t (nm) = (142 ± 8)A. This implies an absorption coefficient of graphene films to be $\alpha=7\times10^{6}$ m^{-1}. This relationship is extremely useful as it allows the transmission scanner to be used to directly measure thickness. To illustrate this, we have converted the right axis of Figure 2D to thickness allowing a direct visualisation of the shape of the traces.

The inset of Figure 2E plots the ratio of peak to trough absorbance values, $A_{peak} / A_{trough} = t_{peak} / t_{trough}$. The data reveals that for the given print settings and drop spacing the peak to trough thickness ratio was ≈1.3, independent of N. We can use the scanner to accurately characterise the cross-sectional profile of the printed lines as shown in Figure 2F. This shows the lines to be very boxlike, even after 4 passes.

It is likely that printed graphene traces will be used predominately for electrical applications. It is envisaged that graphene traces, printed on soft, flexible substrates will be used as electrodes in a range of flexible electronic devices. Indeed printed graphene has already found electrode applications in supercapacitors[24, 25], organic field effect transistors[26] and gas sensors.[19] Especially in flexible electronics it will be important to generate electrode conductivities which are as high as possible for processing temperatures that are as low as possible. Here, the maximum processing temperature was 70 °C which is extremely promising for flexible electronics applications. This makes it important to fully characterise the electrical properties of the structures printed in this work.

Shown in Figure 3 A-C are the measured resistances of printed lines as a function of A) Length, L, (w=2 mm, N=10 kept constant), B) width, w, (L=10 mm, N=10 kept constant) and C) number of print passes, N (w=2 mm, L=20mm kept constant). We find the resistance to scale with both line length and width as expected for a bulk Ohmic material obeying $R = L(\sigma wt)^{-1}$. This behaviour is observed over a decade in L and two decades in w which implies the printing process to give a uniform, continuous material. However, when varying the number of passes, N, the expected behaviour (i.e. $R \propto 1/t \propto 1/N$) is only observed for N≥8. For N<8, the resistance increases with decreasing N much faster than would be expected for a bulk-like material. Such behaviour is due to percolation effects[53] and has been observed previously for inkjet printed graphene traces by a number of authors[22, 23, 28, 31] (although it was analysed only by Torrisi et al[31]). This behaviour will be analysed in more detail below. The data collected in Figure 3 A-C were not all prepared during the same print run or using the same cartridge. To assess the reproducibility of the printing process, we plot the measured resistance for all analysed traces versus $L(wt)^{-1}$ (N was transformed into t using the expression above). We find, that with the exception of the percolative traces mentioned above, all data fall on the same master curve, consistent with σ=3000 S/m. This indicates that the printing process is repeatable, giving reproducible electrical properties for different cartridges, using different batches of graphene ink.

As described above for N<8, the resistance deviates from that expected for a bulk-like material (i.e. one with thickness independent conductivity). Such behaviour occurs when a network of conducting objects is continuously built up. When a very small number of conducting objects is deposited on a surface, no continuous conducting path is formed and the electrical conductivity of the surface is zero. However, at some critical number density the first conducting path is formed and the conductivity becomes non-zero.[53] Percolation theory shows that above this critical number density, N_c, (the percolation threshold), the conductivity scales with conductor number density, N, as $\sigma \propto (N - N_c)^n$ where n is the percolation exponent. In many cases it is convenient to think in terms of network thickness, t, rather than number density. In that case, the network conductivity will depend on t as:[54, 55]

$$\sigma \propto (t - t_c)^n \qquad \text{Equation 1}$$

where t_c is the critical thickness for the onset of conductivity.

Shown in Figure 3E is a plot of network conductivity ($\sigma = L(Rwt)^{-1}$) versus network thickness, t (both calculated using t (nm) = 21×N). As the thickness was increased from 21 to 160 nm, the conductivity increased non-linearly with t. The data is fitted well by Equation 2 with a value of t_c=30 nm and n = 0.32. This critical thickness is equivalent to N between 1 and 2, implying that under these conditions, 1 pass is not enough to generate a continuous conductive path over the length of the trace. Interestingly, the value of n is much lower than the expected universal percolation exponent of 1.3.[53] In fact, the observed percolation exponent for thin graphene networks is almost always greater than 2.[55] However, such behaviour is not unusual for thin nanotube networks where exponents as low as 0.3 have been observed.[55] As expected,[54] the percolation fit breaks down at a value of t_{min} = 160 nm (N~8 passes), above which bulk-like behaviour (i.e. thickness independent conductivity) is observed, consistent with σ=3000 S/m.

We believe the electrical performance of these lines is competitive with previous reports on the conductivity of graphene networks. The maximum conductivity observed for solution processed graphene films tends to be ~2×10^4 S/m.[34] Indeed, conductivities close to this have been reported for inkjet printed graphene lines,[27] although most papers report lower conductivities.[19, 22-26, 28, 29, 31] However, most studies on inkjetted graphene lines involve either a thermal anneal or a chemical treatment which seems to be necessary to achieve the reported conductivity (see SI). In general the conductivity appears to scale with the annealing temperature (Figure 3F and SI). The only cases of high conductivity coupled with low processing temperatures are for graphene oxide lines which have to be reduced in hydrazine.[28, 29] The requirement for such chemical treatments will certainly limit the applications available to such materials. On the contrary, the lines studied here require temperatures no higher than 70 °C and no chemical treatment. We believe this will be a considerable advantage in many applications in flexible electronics.

We believe the ability to achieve good conductivities without thermal or chemical post-treatments is largely due to our graphene exfoliation method. Liquid phase exfoliation gives graphene that is free of defects and oxides.[43, 44, 49] This means the flakes themselves are conductive without any requirement to reduce the material (either thermally of chemically) as is the case with graphene oxide. This means the sample needs to be heated only to 60 °C during printing in order to facilitate solvent drying. Such temperatures are compatible with almost all plastics and organics.

One of the major advantages of inkjet printing of nano-materials is that one can envisage printing of entire devices using combinations of different nano-materials. To this end, using inks prepared by liquid exfoliation of layered crystals is hugely advantageous. This procedure has been used prepare dispersions of nanosheets of many types including BN,[56-58] MoS_2, WS_2, $MoSe_2$ (and other transition metal dichalcogenides),[48, 56, 59-62] MnO_2 [ref [62]] and MoO_3 [ref [63]]. This will allow the printing of a wide range of 2D nano-materials for a broad cohort of applications.

To demonstrate this, we prepared dispersions of NMP-exfoliated[56] MoS_2 nanosheets using a procedure similar to that for graphene. A TEM image of a typical nanosheet and TEM-derived nanosheet size statistics are shown in Figure 4A&B. MoS_2 is a semiconductor[37] with thin films of exfoliated nanosheets known to display photoconductive properties.[64] As such we opted to demonstrate an all inkjet printed photodetector with interdigitated graphene electrodes and an MoS_2 channel. To do this, we first printed the MoS_2 channel in a zigzag pattern as shown in Figure 4C (N=30). Here the channel length (i.e. the inter-electrode spacing) was 1mm while the channel width (i.e. the total contour length of the zigzag) depended on the number of repeating turns of the zigzag but was up to 60 cm for a thirty turn zigzag. Then, graphene electrodes were printed either side of the channel to form an interdigited array (N=10, Figure 4C). The graphene fingers were ~800 μm wide while the thickness of the graphene electrodes was ~215 nm. We note that the graphene electrode was printed to overlap the MoS_2 channel slightly (~100 μm) to ensure good physical contact between graphene and MoS_2 at the interface. Shown in Figure 4D is an optical image of a section of MoS_2 channel. Here, the interface between graphene and MoS_2 looks extremely clean and uniform. This is confirmed by SEM imaging in Figure 4E and F. In particular, Figure 4F shows the interface to be extremely smooth even on length scales approaching that of the nanosheets themselves. This implies that during the droplet drying process, there was time for some intermingling of graphene and MoS_2 nanosheets in the vicinity of the interface. We expect this to result in extremely good electrical connection between graphene and MoS_2.

Before examining the electrical properties of the printed structure shown in Figure 4C, we must consider the nature of the graphene-MoS_2 contact. The work function of undoped, defect-free graphene depends predominantly on the nanosheet thickness, varying from 4.3 eV (below vacuum) for monolayers to 4.6 eV for nanosheets consisting of >10 monolayers.[65] MoS_2 is generally an n-type semiconductor with Fermi energy ~4.8 eV below

the vacuum level reported for bulk crystals.[66] However, the Fermi energy of exfoliated MoS_2 will depend on degree of doping, with papers quoting values in a wide range from 3.5-4.7 eV below vacuum.[67, 68] For a given degree of doping, we expect the Fermi energy to approach the bulk value as the nanosheet thickness increases. An Ohmic contact will occur if the work function of the graphene electrode lies between the Fermi energy and conduction band edge of the MoS_2,[69] otherwise, a Schottky barrier will be formed. Thus, forming an Ohmic contact clearly depends on the thicknesses of both graphene and MoS_2 nanosheets. With this in mind, we expect to find local Ohmic contacts where adjacent graphene and MoS_2 nanosheets both have thicknesses in the appropriate range.

We measured the current-voltage (IV) characteristic (in the dark) for this system observing good linearity as well as symmetry about the origin. This is consistent with an Ohmic contact between the graphene and MoS_2, implying the current injection to be dominated by the local Ohmic contacts. The (dark) resistance of the system was $\sim 2\times10^{10}$ Ω. From their geometry, we expect the electrodes to contribute no more than 100 kΩ to this, meaning the observed resistance is completely dominated by the MoS_2. This implies a conductivity of $\sim 2.5\times10^{-6}$ S/m for the MoS_2 film, close to previous reports of the in-plane conductivity of solution-processed MoS_2 films (7×10^{-7} S/m).[70]

In order to explore the photoconductivity of this system, we measured IV curves while illuminating the sample with a laser (532 nm, 2.3 eV). This laser was chosen to allow excitation of band to band transitions given the bandgap of fully exfoliated MoS_2 is ~1.9 eV.[71] In all cases, IV curves were recorded once the photocurrent had reached its steady state value for each value of intensity. Shown in Figure 4G are IV curves for a range of incident intensities up to 640 mW/cm^2. It is clear that a considerable photocurrent is generated in these systems. The conductance, G, is plotted as a function of incident intensity in Figure 4H. We observe a tenfold increase compared to the dark conductance for an intensity of 640 mW/cm^2. This suggests that such structures are viable for use as low-end photodetectors.

The photoconductivity increases supra-linearly with intensity as can be found occasionally throughout the literature.[72] This is consistent with the presence of defect levels within the forbidden energy gap with a larger cross-section for capture of minority carriers. This prolongs majority carrier lifetime as the intensity increases.[69] A two defect level model can be employed to explain these phenomenon. Depending on the illumination intensity we see other two level phenomena such as photocurrent quenching and, at low intensity, negative

photoconductivity (not shown).[73,74] These interesting effects will be explored in a future paper.

In summary, we have demonstrated inkjet printing of liquid exfoliated graphene onto a commercial pre-treated PET without the need for additional surface treatment or annealing above 70 °C. We have generated well-defined traces with controllable width, length and thickness. These traces act like Ohmic conductors with conductivity ~3000 S/m so long as the trace thickness is above 160 nm. Below this thickness percolation effects begin to dominate. The same procedure can be used to print traces from liquid exfoliated MoS_2. We have combined MoS_2 and graphene structures in an all-inkjet printed interdigitated electrode/channel structure. We found this process to give extremely clean and uniform graphene/MoS_2 interfaces. This system worked extremely well as a photodetector, displaying a 10-fold current increase when exposed to 640 mW/cm^2 incident laser illumination.

Experimental Methods

The graphene ink was obtained by sonicating pristine graphite (SGN-18 from FutureCarbon GmbH) in the solvent N-methyl pyrrolidone (ReagentPlus 99%, Sigma Aldrich). An initial graphite concentration of 75 mg/ml was processed for 7 hours in 100 ml NMP using a horn tip sonicator (Sonics Vibra-cell VCX-750 ultrasonic processor) operating at 40% amplitude. The dispersion was processed inside a stainless steel flask with cooling provided by immersion in an ice water bath. This dispersion was then diluted by addition of 100 mL of fresh NMP and sonicated for a further 30 minutes at 70% amplitude. After sonication, the dispersion was centrifuged using a Hettich Mickro 22R for 60 minutes at 3500 RPM. The top 12 ml of the dispersion was removed and centrifuged again under identical conditions. This procedure gives small graphene nanosheets dispersed at low concentration in a relatively large volume of NMP.

To raise the concentration of the graphene ink the dispersion was centrifuged at 12000 RPM for 90 minutes in a Thermo Fisher Scientific Megafuge 16. This process left a pale grey supernatant with the majority of graphene flakes at the bottom of the vials. The sediment was extracted and briefly redispersed by sonication in 0.5 ml NMP using a sonic bath. UV-Vis spectrometry was used to measure A_{660}/l = 26,100 m^{-1} for the concentrated ink. Thus, the concentration of the ink was measured as C_{ink} = 6.22 mg/ml, using the extinction coefficient of 4200 L mg^{-1} mL^{-1}.

Printing of conductive patterns was performed using a Dimatix inkjet printer with a printhead consisting of 16 inkjet nozzles. To avoid blockage of the nozzles during operation and in standby mode, the graphene/NMP ink was diluted to an optimum concentration of 1.55 mg/ml. To avoid substrate-related drying problems, we tested a number of substrates before settling on a semi-transparent coated PET material from Mitsubishi Paper Mills Ltd (NB-TP-3GU100). This material consisted of PET coated with aluminium oxide and polyvinyl alcohol and is generally used for the inkjet printing of water-based silver nanoparticle ink.

Before inkjet printing, the coated PET substrate was placed on a vacuum heated platen in the printer which can be set to a maximum temperature of 60 °C. The temperature of the NMP fluid in the printhead was raised above ambient (max. 70 °C) to lower the viscosity and to optimize the desired jetting performance. In order to achieve high-quality results, it is very important to optimise the printing conditions. A detailed description is given in the supporting information.

The graphene ink was characterised by optical absorption spectroscopy (Varian Cary 6000i) and transmission electron microscopy (Jeol 2100). Qualitative analysis of the inkjet-printed traces on each substrate was carried out using a Zeiss measuring microscope (Axio Imager M1m). Raman was performed using a WITec Confocal Raman Microscopy Alpha 300 R using a 20-100× objective lens with a 532.15 nm laser excitation. The fabricated graphene traces on coated PET were characterized using a Carl Zeiss Ultra Plus scanning electron microscope. The graphene film thickness was measured using a flatbed optical scanner (Epson Perfection V700 Photo flatbed transmission scanner with a bit depth of 48-bits per pixel and a spatial resolution of 6400 dpi) in conjunction with height measurement data from a profilometer (Dektak 6M profilometer). The electrical characterization was performed using a Keithley 2400 source meter.

For the photoconductivity experiments, the printing was performed on Teslin, a waterproof, microporous synthetic printing substrate. During laser illumination (Coherent Verdi DPSS, 532 nm), a beam expander was used to ensure the whole sample area (1 cm×2 cm in this case, including both graphene and MoS_2 regions) was illuminated. We note that, prior to photoconductivity experiments the sample was annealed for 2 hours under vacuum at 200 ^{o}C. This was not to improve the conductivity of the printed graphene; rather it is known that such an anneal reduces noise in solution processed MoS_2 photodetectors.[64] Thus, this is

an application-specific anneal and will not be necessary for all applications of inkjet printed graphene electrodes.

Acknowledgements

We acknowledge the European Research Council grant SEMANTICS for financial support and thank Richard Coull for extensive help and advice. JNC acknowledges support by the EC under the Graphene Flagship (contract no. CNECT-ICT-604391).

Figures

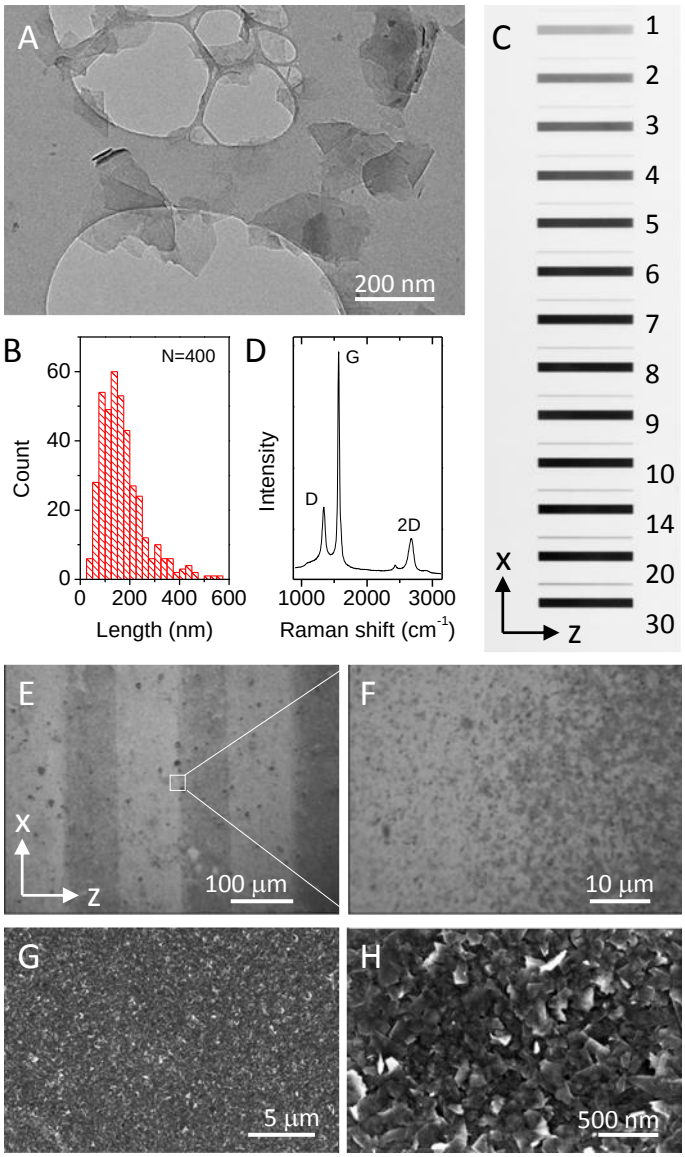

Figure 1: A) TEM image of liquid exfoliated graphene nanosheets. B) Length distribution histogram for nanosheets used in this work (400 nanosheets counted). C) Photograph of printed graphene traces for different number of passes, N, as shown on the image. These traces have lateral dimensions: w=2 mm and L=20 mm. The x and z directions are included to allow comparison with Figures 1E and 2A. D) Raman spectrum taken for one of the trace (N=30). E) Optical micrograph of a thin trace (N=5). F) Zoomed image of the edge of the trace in E. G&H) SEM images of the centre of a thicker trace (N=20).

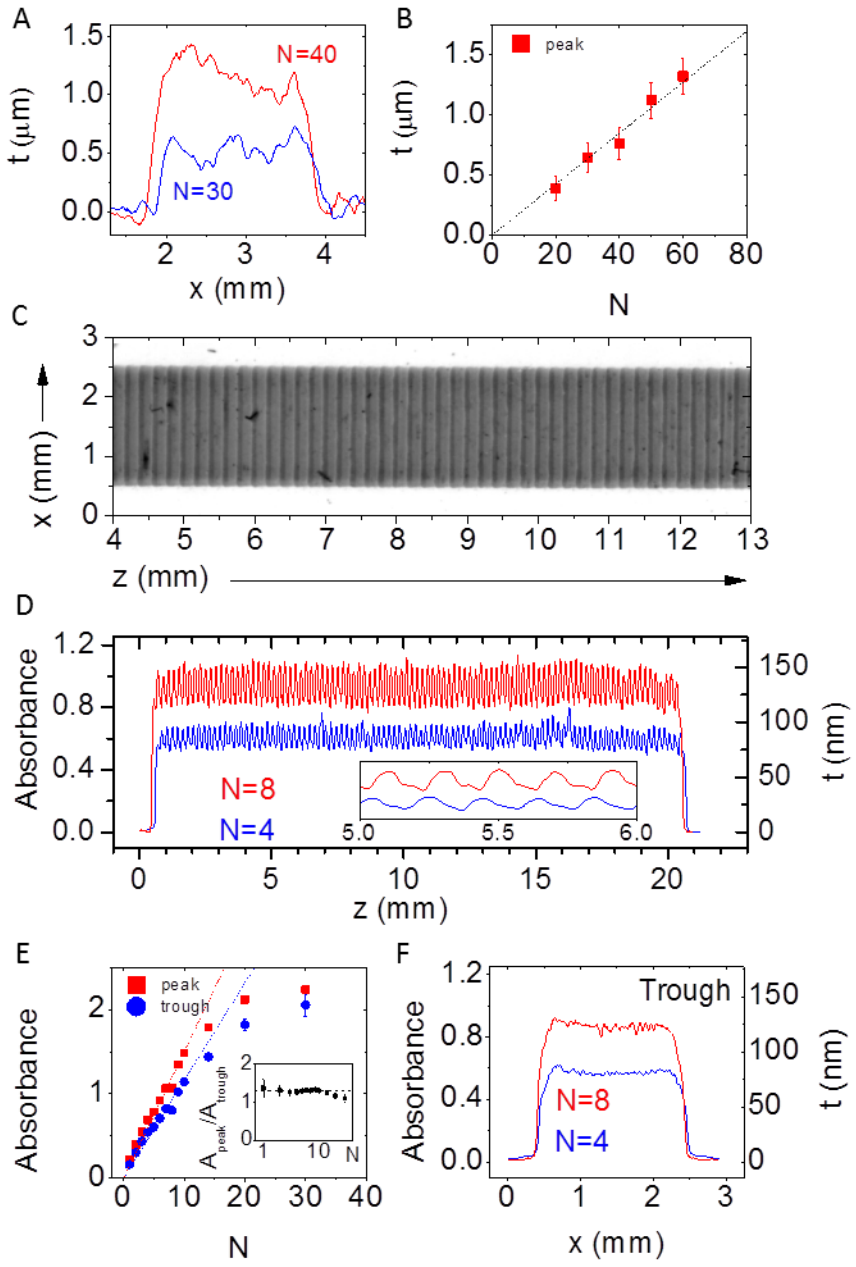

Figure 2: A) Examples of profilometry line profiles for two traces with N=30 and N=40. B) Trace height (measured at peak of striations) plotted as a function of number of passes, N. C) Scanner image of a section of a thin trace (N=1), clearly showing striations. D) Absorbance line profile taken across the full length of two traces with N=4 and N=8. N.B. in the right axis, absorbance has been converted to thickness. Inset: High resolution line profiles showing the apparent "noise" in the main panel to be due to striations with spatial period of 200 μm. E) Local absorbance, measured both at peak and trough of striations, plotted as a function of number of passes, N. Inset: Ratio of peak to trough absorbance as a function of N. F) Absorbance line profile taken across the width of two traces with N=4 and N=8. These

measurements were taken in the trough between striations. N.B. in the right axis, absorbance has been converted to thickness.

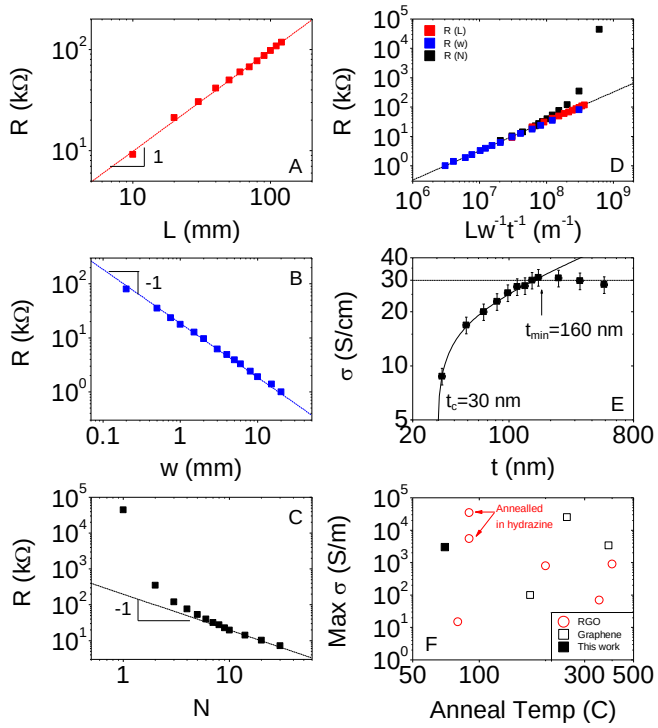

Figure 3: A-C) Resistance of printed lines as a function of A) Length, L, (w=2 mm, N=10), B) width, w, (L=10 mm, N=10) and C) number of print passes, N (w=2 mm, L=20mm). The dashed lines represent the behaviour expected for a bulk-like material. D) Resistance of printed lines as a function of $Lw^{-1}t^{-1}$. Linear behaviour is expected for bulk-like materials as illustrated by the dashed line. E) Electrical conductivity, σ, plotted as a function of line thickness, t. Above a threshold thickness, t_{min}, the conductivity is thickness independent as expected for a bulk-like material. Below t_{min}, the conductivity is thickness dependent and is described by percolation theory (i.e. equation 1, solid line) with percolation exponent, n=0.32 and percolation threshold, t_c=30 nm. F) Survey of literature describing electrical properties of inkjet printed graphene. The data is divided into reduced graphene oxide (RGO) and graphene exfoliated directly from graphite. The references for these data are given in the SI.

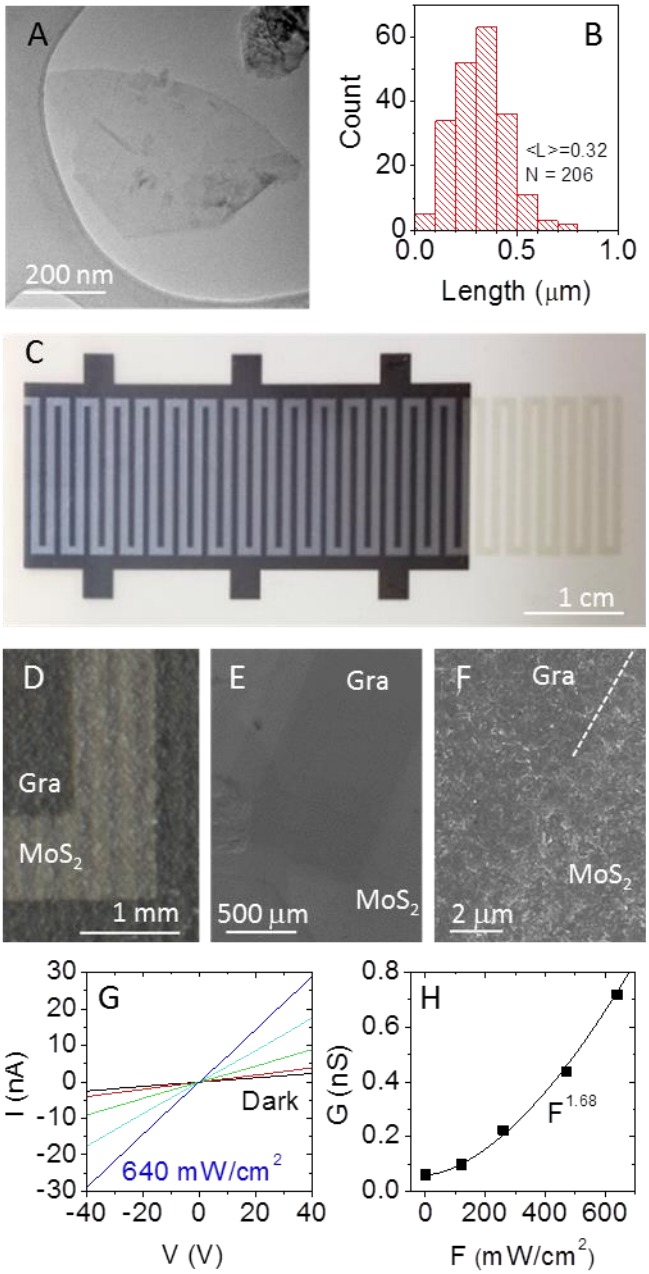

Figure 4: A) Representative TEM image and B) nanosheet size distribution for size selected MoS_2 nanosheets. C) Photograph of printed photodetector. The black regions are the graphene interdigitated electrodes (N=30). The yellow/green zigzag structure is MoS_2. The darker portions represent 30 print passes while the yellow region stretching beyond the graphene electrodes was printed using 1 pass and was produced for visualisation purposes. D-F) An optical image (D) and SEM images (E-F) showing the graphene/MoS_2 interface. The dashed line in F illustrates the position of the interface. G) Current-voltage curves for the photodetector in the dark and under various illuminations up to 640 mW/cm^2. H) Measured conductance (G) plotted versus incident intensity (F).

References

1. I. M. Hutchings and G. D. Martin, *Inkjet technology for digital fabrication*, John Wiley & Sons, Chichester, West Sussex, 2013.
2. H. Yan, Z. H. Chen, Y. Zheng, C. Newman, J. R. Quinn, F. Dotz, M. Kastler and A. Facchetti, *Nature*, 2009, **457**, 679-U671.
3. A. D. Del Mauro, R. Diana, I. A. Grimaldi, F. Loffredo, P. Morvillo, F. Villani and C. Minarini, *Polymer Composites*, 2013, **34**, 1493-1499.
4. C. N. Hoth, S. A. Choulis, P. Schilinsky and C. J. Brabec, *Advanced Materials*, 2007, **19**, 3973-+.
5. V. Wood, M. J. Panzer, J. L. Chen, M. S. Bradley, J. E. Halpert, M. C. Bawendi and V. Bulovic, *Advanced Materials*, 2009, **21**, 2151-+.
6. H. H. Lee, K. S. Chou and K. C. Huang, *Nanotechnology*, 2005, **16**, 2436-2441.
7. P. Kossyrev, *Journal of Power Sources*, 2012, **201**, 347-352.
8. W. R. Small and M. I. H. Panhuis, *Small*, 2007, **3**, 1500-1503.
9. H. Sirringhaus, T. Kawase, R. H. Friend, T. Shimoda, M. Inbasekaran, W. Wu and E. P. Woo, *Science*, 2000, **290**, 2123-2126.
10. J. Zhang, Y. Zhao, Z. M. Wei, Y. M. Sun, Y. D. He, C. A. Di, W. Xu, W. P. Hu, Y. Q. Liu and D. B. Zhu, *Advanced Functional Materials*, 2011, **21**, 786-791.
11. J. Bharathan and Y. Yang, *Applied Physics Letters*, 1998, **72**, 2660-2662.
12. C. N. Hoth, P. Schilinsky, S. A. Choulis and C. J. Brabec, *Nano Letters*, 2008, **8**, 2806-2813.
13. P. C. Chen, H. T. Chen, J. Qiu and C. W. Zhou, *Nano Research*, 2010, **3**, 594-603.
14. C. Karuwan, C. Sriprachuabwong, A. Wisitsoraat, D. Phokharatkul, P. Sritongkham and A. Tuantranont, *Sensors and Actuators B-Chemical*, 2012, **161**, 549-555.
15. O. Monereo, S. Claramunt, M. M. de Marigorta, M. Boix, R. Leghrib, J. D. Prades, A. Cornet, P. Merino, C. Merino and A. Cirera, *Talanta*, 2013, **107**, 239-247.
16. M. Mantysalo and P. Mansikkamaki, *Aeu-International Journal of Electronics and Communications*, 2009, **63**, 31-35.
17. A. K. Geim, *Science*, 2009, **324**, 1530-1534.
18. K. S. Novoselov, V. I. Fal'ko, L. Colombo, P. R. Gellert, M. G. Schwab and K. Kim, *Nature*, 2012, **490**, 192-200.
19. V. Dua, S. P. Surwade, S. Ammu, S. R. Agnihotra, S. Jain, K. E. Roberts, S. Park, R. S. Ruoff and S. K. Manohar, *Angewandte Chemie-International Edition*, 2010, **49**, 2154-2157.
20. R. Giardi, S. Porro, A. Chiolerio, E. Celasco and M. Sangermano, *Journal of Materials Science*, 2013, **48**, 1249-1255.
21. J. T. Han, J. S. Kim, D. Kwak, B. G. Kim, B. H. Jeong, S. Y. Jeong, H. J. Jeong, K. Cho and G. W. Lee, *Rsc Advances*, 2011, **1**, 44-47.
22. L. Huang, Y. Huang, J. J. Liang, X. J. Wan and Y. S. Chen, *Nano Research*, 2011, **4**, 675-684.
23. D. Kong, L. T. Le, Y. Li, J. L. Zunino and W. Lee, *Langmuir*, 2012, **28**, 13467-13472.
24. L. T. Le, M. H. Ervin, H. W. Qiu, B. E. Fuchs and W. Y. Lee, *Electrochemistry Communications*, 2011, **13**, 355-358.
25. J. Li, F. Ye, S. Vaziri, M. Muhammed, M. C. Lemme and M. Ostling, *Advanced Materials*, 2013, **25**, 3985-3992.
26. S. Lim, B. Kang, D. Kwak, W. H. Lee, J. A. Lim and K. Cho, *Journal of Physical Chemistry C*, 2012, **116**, 7520-7525.
27. E. B. Secor, P. L. Prabhumirashi, K. Puntambekar, M. L. Geier and M. C. Hersam, *Journal of Physical Chemistry Letters*, 2013, **4**, 1347-1351.
28. K. Y. Shin, J. Y. Hong and J. Jang, *Advanced Materials*, 2011, **23**, 2113-+.
29. K. Y. Shin, J. Y. Hong and J. Jang, *Chemical Communications*, 2011, **47**, 8527-8529.
30. C. Sriprachuabwong, C. Karuwan, A. Wisitsorrat, D. Phokharatkul, T. Lomas, P. Sritongkham and A. Tuantranont, *Journal of Materials Chemistry*, 2012, **22**, 25501-25503.
31. F. Torrisi, T. Hasan, W. P. Wu, Z. P. Sun, A. Lombardo, T. S. Kulmala, G. W. Hsieh, S. J. Jung, F. Bonaccorso, P. J. Paul, D. P. Chu and A. C. Ferrari, *Acs Nano*, 2012, **6**, 2992-3006.

32. Y. Yu, H. Wada, J. Inoue, S. Imaizumi, Y. Kounosu, K. Tsuboi, H. Matsumoto, M. Ashizawa, T. Mori, M. Minagawa and A. Tanioka, *Applied Physics Express*, 2011, **4**.
33. H. Zhang, A. J. Xie, Y. H. Shen, L. G. Qiu and X. Y. Tian, *Physical Chemistry Chemical Physics*, 2012, **14**, 12757-12763.
34. S. De and J. N. Coleman, *Acs Nano*, 2010, **4**, 2713-2720.
35. V. Nicolosi, M. Chhowalla, M. G. Kanatzidis, M. S. Strano and J. N. Coleman, *Science*, 2013, **340**, 1420-+.
36. M. Chhowalla, H. S. Shin, G. Eda, L. J. Li, K. P. Loh and H. Zhang, *Nat. Chem.*, 2013, **5**, 263-275.
37. Q. H. Wang, K. Kalantar-Zadeh, A. Kis, J. N. Coleman and M. S. Strano, *Nature Nanotechnology*, 2012, **7**, 699-712.
38. X. Huang, X. Y. Qi, F. Boey and H. Zhang, *Chemical Society Reviews*, 2012, **41**, 666-686.
39. X. Huang, Z. Y. Yin, S. X. Wu, X. Y. Qi, Q. Y. He, Q. C. Zhang, Q. Y. Yan, F. Boey and H. Zhang, *Small*, 2011, **7**, 1876-1902.
40. X. Huang, Z. Y. Zeng and H. Zhang, *Chemical Society Reviews*, 2013, **42**, 1934-1946.
41. P. Blake, P. D. Brimicombe, R. R. Nair, T. J. Booth, D. Jiang, F. Schedin, L. A. Ponomarenko, S. V. Morozov, H. n. F. Gleeson, E. W. Hill, A. K. Geim and K. S. Novoselov, *Nano Letters*, 2008, **8**, 1704-1708.
42. A. B. Bourlinos, V. Georgakilas, R. Zboril, T. A. Steriotis and A. K. Stubos, *Small*, 2009, **5**, 1841-1845.
43. J. N. Coleman, *Accounts of Chemical Research*, 2013, **46**, 14-22.
44. Y. Hernandez, V. Nicolosi, M. Lotya, F. M. Blighe, Z. Sun, S. De, I. T. McGovern, B. Holland, M. Byrne, Y. K. Gun'ko, J. J. Boland, P. Niraj, G. Duesberg, S. Krishnamurthy, R. Goodhue, J. Hutchison, V. Scardaci, A. C. Ferrari and J. N. Coleman, *Nature Nanotechnology*, 2008, **3**, 563-568.
45. A. A. Green and M. C. Hersam, *Nano Letters*, 2009, **9**, 4031-4036.
46. M. Lotya, Y. Hernandez, P. J. King, R. J. Smith, V. Nicolosi, L. S. Karlsson, F. M. Blighe, S. De, Z. M. Wang, I. T. McGovern, G. S. Duesberg and J. N. Coleman, *Journal of the American Chemical Society*, 2009, **131**, 3611-3620.
47. A. B. Bourlinos, V. Georgakilas, R. Zboril, T. A. Steriotis, A. K. Stubos and C. Trapalis, *Solid State Commun.*, 2009, **149**, 2172-2176.
48. P. May, U. Khan, J. M. Hughes and J. N. Coleman, *Journal of Physical Chemistry C*, 2012, **116**, 11393-11400.
49. U. Khan, A. O'Neill, M. Lotya, S. De and J. N. Coleman, *Small*, 2010, **6**, 864-871.
50. A. C. Ferrari, J. C. Meyer, V. Scardaci, C. Casiraghi, M. Lazzeri, F. Mauri, S. Piscanec, D. Jiang, K. S. Novoselov, S. Roth and A. K. Geim, *Physical Review Letters*, 2006, **97**.
51. P. J. Lyon, J. Carter, C. Creighton and H. Gregory, *Solvents for Pedot-Solutions for Inkjet Printing*, US patent application 2009/0121618, 2009.
52. J. Castano and X. Girones, *Method of reducing vertical banding in ink jet printing*, U.S. Patent 6,595,621, 2003.
53. D. S. Stauffer and A. Aharony, *Introduction to percolation theory*, Taylor and Francis, London, 1994.
54. S. De, P. J. King, P. E. Lyons, U. Khan and J. N. Coleman, *Acs Nano*, 2010, **4**, 7064-7072.
55. S. De and J. N. Coleman, *Mrs Bulletin*, 2011, **36**, 774-781.
56. J. N. Coleman, M. Lotya, A. O'Neill, S. D. Bergin, P. J. King, U. Khan, K. Young, A. Gaucher, S. De, R. J. Smith, I. V. Shvets, S. K. Arora, G. Stanton, H. Y. Kim, K. Lee, G. T. Kim, G. S. Duesberg, T. Hallam, J. J. Boland, J. J. Wang, J. F. Donegan, J. C. Grunlan, G. Moriarty, A. Shmeliov, R. J. Nicholls, J. M. Perkins, E. M. Grieveson, K. Theuwissen, D. W. McComb, P. D. Nellist and V. Nicolosi, *Science*, 2011, **331**, 568-571.
57. Y. Lin, T. V. Williams and J. W. Connell, *Journal of Physical Chemistry Letters*, 2010, **1**, 277-283.
58. C. Y. Zhi, Y. Bando, C. C. Tang, H. Kuwahara and D. Golberg, *Advanced Materials*, 2009, **21**, 2889-+.
59. G. Cunningham, M. Lotya, C. S. Cucinotta, S. Sanvito, S. D. Bergin, R. Menzel, M. S. P. Shaffer and J. N. Coleman, *ACS Nano*, 2012, **6**, 3468-3480.

60. A. O'Neill, U. Khan and J. N. Coleman, *Chemistry of Materials*, 2012, **24**, 2414-2421.
61. K. G. Zhou, N. N. Mao, H. X. Wang, Y. Peng and H. L. Zhang, *Angewandte Chemie-International Edition*, 2011, **50**, 10839-10842.
62. R. J. Smith, P. J. King, M. Lotya, C. Wirtz, U. Khan, S. De, A. O'Neill, G. S. Duesberg, J. C. Grunlan, G. Moriarty, J. Chen, J. Z. Wang, A. I. Minett, V. Nicolosi and J. N. Coleman, *Advanced Materials*, 2011, **23**, 3944-+.
63. D. Hanlon, C. Backes, M. Hughes, A. O'Neill, P. King, T. Higgins, N. McEvoy, G. S. Duesberg, B. Mendoza-Sanchez, V. Nicolosi and J. N. Coleman, *in preparation*, 2013.
64. G. Cunningham, U. Khan, C. Backes, D. Hanlon, D. McCloskey, J. Donegan and J. N. Coleman, *Journal of Materials Chemistry C*, 2013, **in press**, DOI: 10.1039/C1033TC31402B.
65. H. Hibino, H. Kageshima, M. Kotsugi, F. Maeda, F. Z. Guo and Y. Watanabe, *Physical Review B*, 2009, **79**.
66. T. Shimada, F. S. Ohuchi and B. A. Parkinson, *Jpn. J. Appl. Phys., Part 1,*, 1994, **33**, 2696-2698.
67. Z. Y. Yin, H. Li, L. Jiang, Y. M. Shi, Y. H. Sun, G. Lu, Q. Zhang, X. D. Chen and H. Zhang, *Acs Nano*, 2012, **6**, 74-80.
68. L. T. Liu, S. B. Kumar, Y. Ouyang and J. Guo, *Ieee Transactions on Electron Devices*, 2011, **58**, 3042-3047.
69. R. H. Bube, *Photoconductivity of Solids*, John Wiley & Sons, New York, 1960.
70. G. Cunningham, M. Lotya, N. McEvoy, G. S. Duesberg, P. van der Schoot and J. N. Coleman, *Nanoscale*, 2012, **4**, 6260-6264
71. A. Kuc, N. Zibouche and T. Heine, *Physical Review B*, 2011, **83**.
72. R. Bube, *Physical Review*, 1955, **99**, 1105-1116.
73. R. H. Bube, *Photoelectronic Properties of Semiconductors*, Cambridge University Press, Cambridge, 1992.
74. A. Serpi, *physica status solidi (a)*, 1992, **133**, K73–K77.